maximum shear stress ($\tau_{max} = \frac{1}{2}(\sigma_1 - \sigma_3)$), which captures the intensity of shear demand generated by contrasts in stiffness, discontinuities, and cavity geometry, and therefore represents the most direct indicator of shear-driven deformation in this context; and (iii) the vertical displacement (u_z), which describes the upward or downward movements associated with roof flexure, local sagging, and vertical adjustments around the carved chambers, providing essential insight into deformation mechanisms that cannot be inferred from stress fields alone.

In addition to external and cavities surfaces analysis, to provide a spatially traceable and assumption-free reading of the model behavior, a total of thirteen cross-sections were extracted from the 3D domain in Rocscience™ RS3 (Version 4.039; **Rocscience™ Inc. 2025**). These sections, later described within the text, comprise seven longitudinal slices aligned with the chambers' development axis (orthogonal to the slope direction), and six inward-parallel slices oriented parallel to the façade, cutting progressively deeper into the rock mass. The cross-section set allows a direct observation of how compressive and shear stress gradients and vertical deformation propagate both inward and along from the chamber openings and façade pillar constraints.

3.2.5.3.1 Major principal stress (σ_1) distribution

Within this framework, the σ_1 field reveals a distinct concentration of compressive stress at the base of the anthropogenic chambers (Figure 3.32, 3.33, and 3.34). This behavior is mechanically consistent with the geometry of the excavated volumes, particularly where domed or arched morphologies are present. The removal of material forces the vertical load to be redistributed laterally, creating abutment zones along the lower margins of the cavity walls and pillars which are mainly excavated in sandstone and, secondarily, in siltstone. These areas act as natural buttresses that channel the stress paths into the surrounding rock mass, resulting in localized σ_1 peaks that reflect load-bearing redistribution rather than an inherent reduction in stability. These σ_1 peaks are not interpreted

as global strength exceedance or slope failure conditions but as evidence of geometrically constrained compressive load redirection affecting both the external cliff surface and the internal cavity walls.

In the zones relevant for stability reading, σ_1 values, ranging from –0.90 to 4.50 MPa, remain predominantly below the intact sandstone compressive strength (35.06 MPa), as reported in the literature reference (**Marinos & Tsiambaos, 2010**), and the uniaxial strength value adopted in this study (14 MPa). This indicates that the stress concentrations reflect geometry-constrained load redirection rather than compressive failure of intact rock. Similarly, the resulting σ_1 values are below the limit of compressive strength for siltstones (i.e., 16.91 MPa) according to **Marinos & Tsiambaos (2010)**.

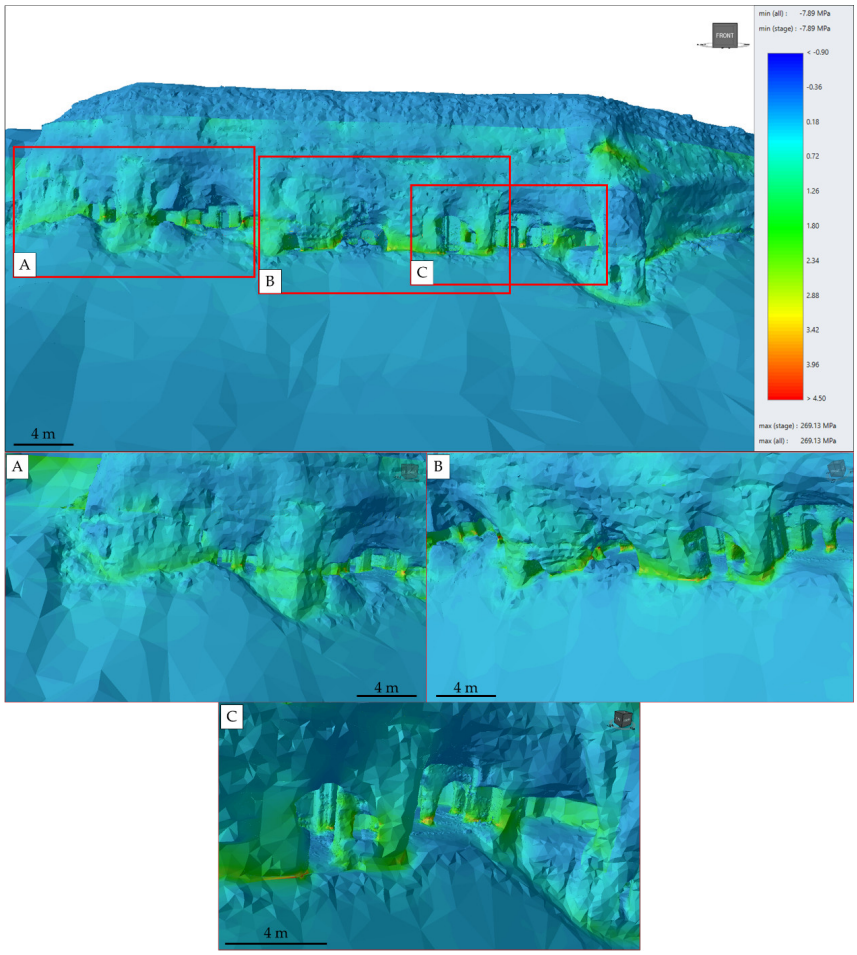

Figure 3.32: Major principal stress (σ_1) distribution on the Sabereebi cliff, with zoomed views (A, B, and C) showing the localized compressive stress concentrations (range: –0.90 to 4.50 MPa).

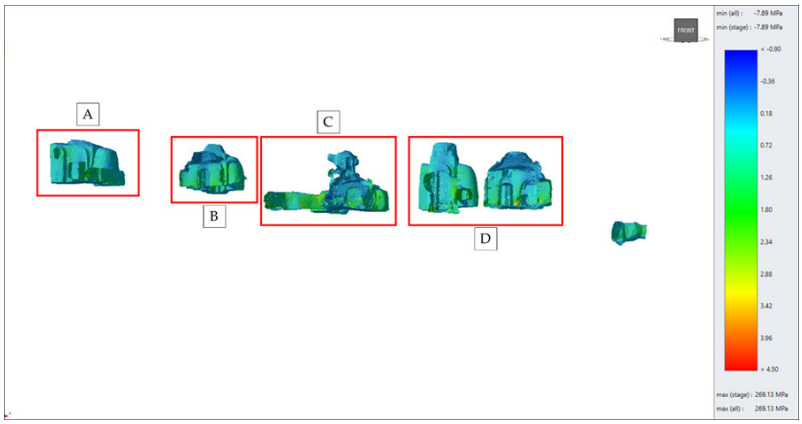

Figure 3.33: Major principal stress (σ_1) distribution around the internal rock-cut chambers.

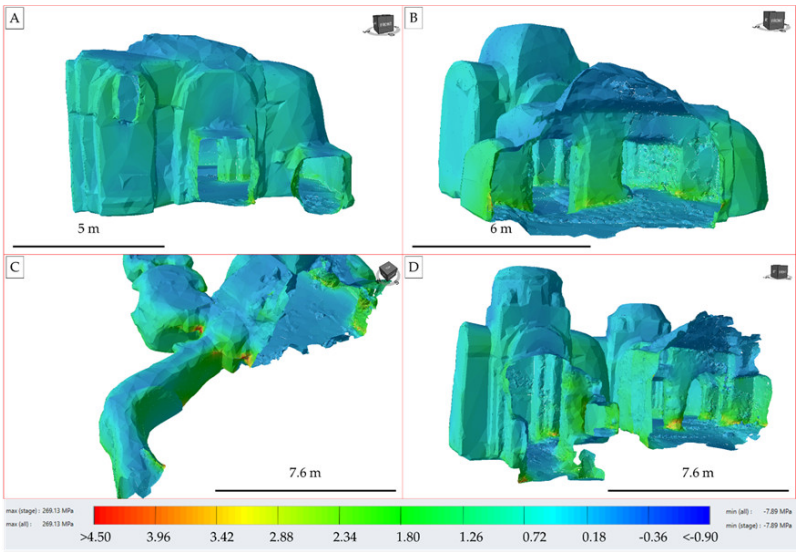

Figure 3.34: Zoomed views of the major principal stress (σ_1) distribution around the internal rock-cut chambers. These views highlight stress concentrations along the lower margins of the excavated volumes. Panel A shows the northwestern chamber, panel B shows its neighbor chamber towards southeast, panel C shows the central chamber, and panel D shows the southeastern most chambers.

3.2.5.3.2 Shear stress (τ) distribution

The distribution of the maximum shear stress (τ) highlights consistent spatial localization of shear demand along the rock–clay slope interface and at the lower margins of the rock-cut chambers (Figure 3.35, 3.36, and 3.37). The highest τ concentrations appear at the bases of vertical façade walls and along the flanks of slender inter-chamber pillars, forming vertically elongated stress lobes that extend a short distance above the clay contact—particularly where geometry imposes lateral constraint and reduced local confinement.

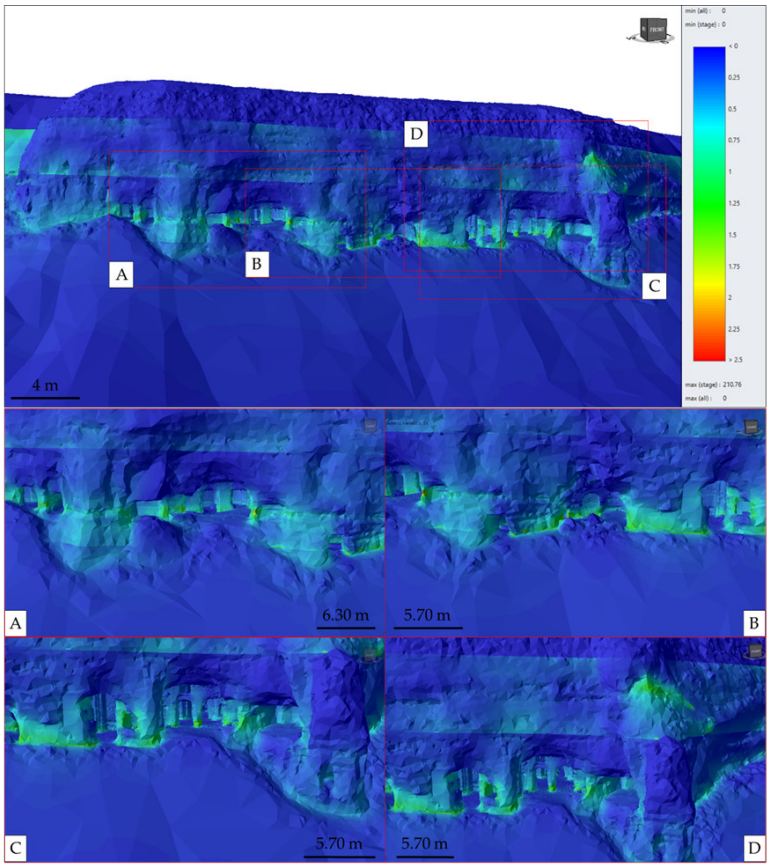

Figure 3.35: Shear stress (τ) distribution on the Sabereebi cliff, with zoomed views (A, B, C, and D) showing the localized shear stress concentrations (range: 0 to 2.50 MPa).

In both the external façade and internal cavity domain, shear stresses remain confined to a localized, geometry-controlled range, with τ values visually spanning from near-zero to, at most, 2 MPa. The dominant transitions occur between 0.75–2 MPa, representing the most recurrent shear-adjustment interval where the rock mass interfaces the open cliff surface and the carved chamber boundaries.

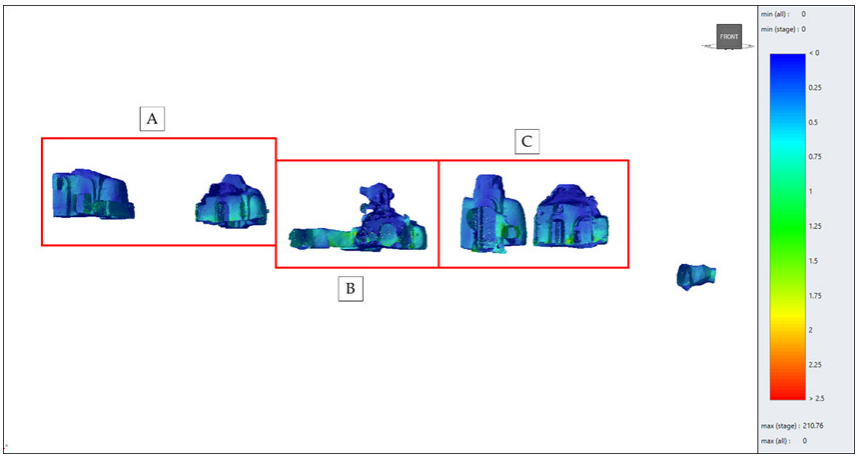

Figure 3.36: Shear stress (τ) distribution in correspondence with the excavated chambers showing the localized shear stress concentrations.

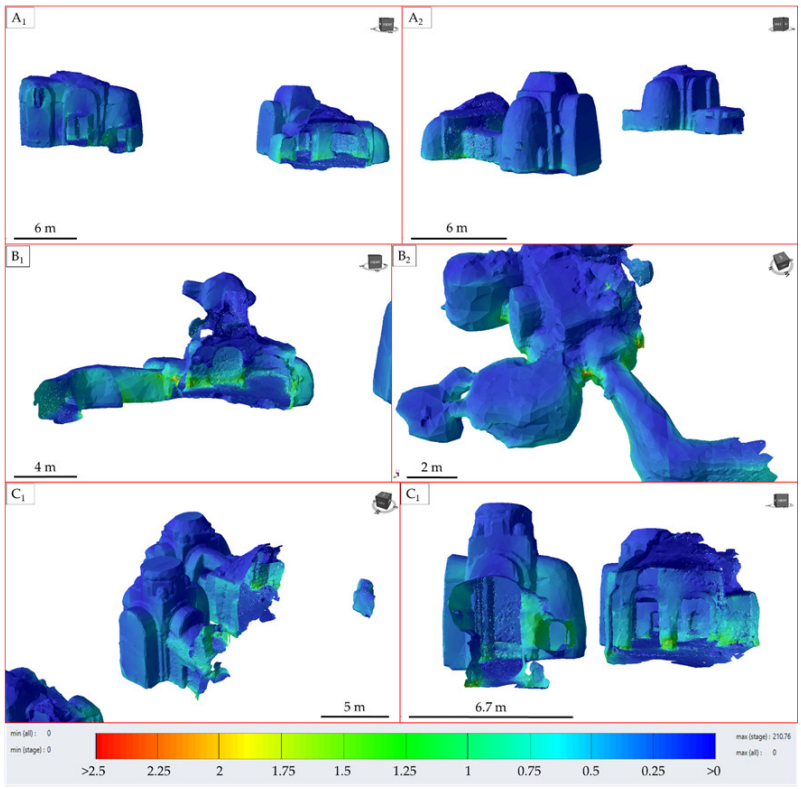

Figure 3.37: Views of shear stress (τ) distribution in correspondence with the excavated chambers showing the localized shear stress concentrations. Panels A1 and A2 show the first two chambers from NW, panels B1 and B2 show the central chamber, and panels C1 and C2 show the two southeastern most chambers. All chambers are shown from two different points of view.

In this model configuration, the basal clay slope unit preserves $\tau \approx 0$ MPa throughout, confirming that all non-zero τ values refer exclusively to overlying rock units and excavation-bounded geometry, without indicating spatially distributed shear rupture through intact model volumes.

3.2.5.3.3 Vertical displacement (u_z) distribution

The vertical displacement (u_z) results were inspected on the external cliff façade and directly around the internal rock-cut cavities (Figures Figure 3.38, 3.39, and 3.40). Vertical displacement values are visually spanning from 0 to -0.29 m (in the soil at the top of the model). In the area of interest, where the rock volume interfaces the open façade and the cavity boundaries, displacements remain confined to a centimetric deformation range, with magnitudes ranging from –0.086 to –0.057 m. In this model setup, the basal clay slope unit preserves $u_z \approx 0$ m throughout, confirming that the vertical deformation component is mechanically null where clay dominates and that all non-zero u_z values refer exclusively to overlying rock volumes and excavation-controlled boundaries.

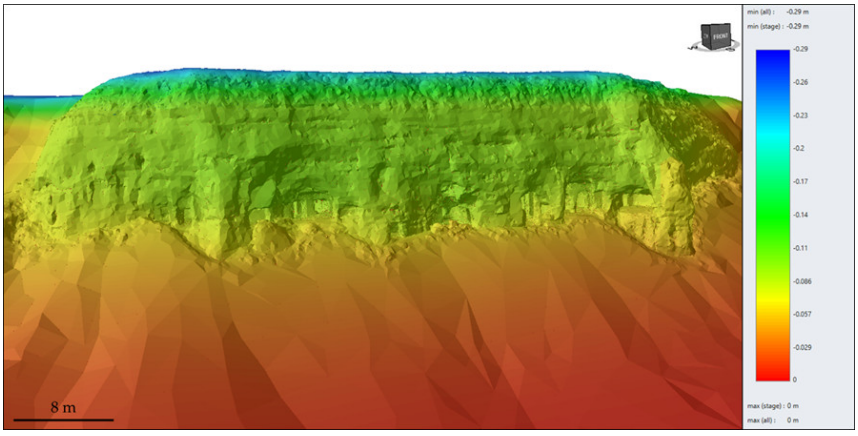

Figure 3.38: Vertical displacement (u_z) distribution on the Sabereebi cliff.

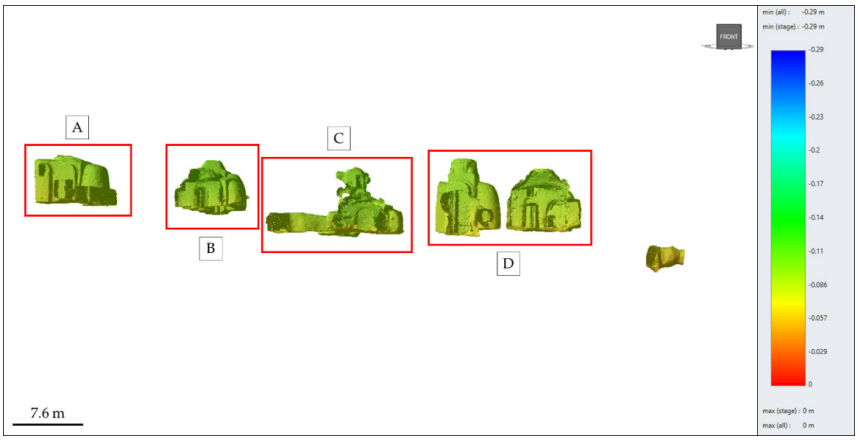

Figure 3.39: Vertical displacement (u_z) distribution in correspondence with the excavated chambers showing the localized variations.

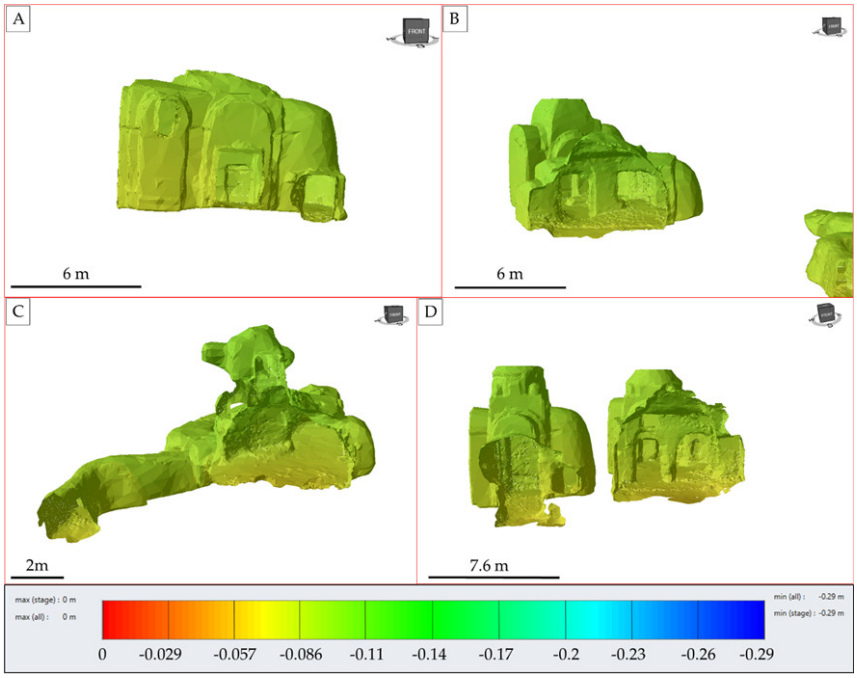

Figure 3.40: Vertical displacement (u_z) distribution around the internal rock-cut chambers. Panel A shows the northwestern chamber, panel B shows its neighbor southwestern chamber, panel C shows the central chamber, and panel D shows the southeastern most chambers.

3.2.5.3.4 Cross-sections analysis

To better analyze how stresses and deformations propagate both across and along the carved chambers, a total of thirteen cross-sections (Figure 3.41) were extracted from the 3D

numerical model. These include seven longitudinal sections aligned with the development axis of the chambers (orthogonal to the slope - Figure 3.41A), and six sections parallel to the cliff face but extending inward into the model (Figure 3.41B), cutting progressively deeper inside the rock mass. The longitudinal sections document the mechanical behavior along the internal extent of the cavities, highlighting tunnel-like stress patterns and the role of pillars and wall segments in constraining deformation. In contrast, the inward-oriented parallel sections provide a transverse perspective on how the façade and the chamber entrances influence stress concentration, shear localization, and vertical settlement as these effects propagate deeper into the slope.

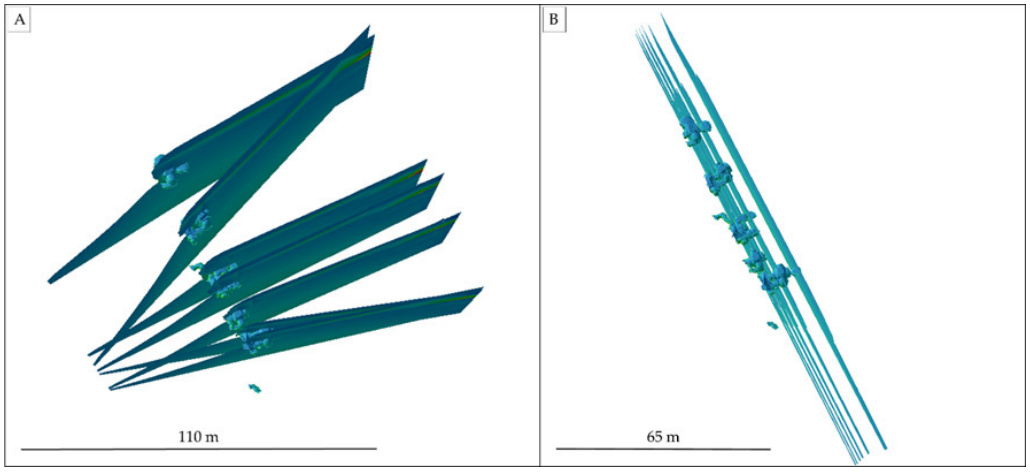

Figure 3.41: Set of thirteen FEM cross-sections: seven longitudinal sections aligned with the chamber axis (A) and six inward-oriented slices parallel to the façade (B).

Major principal stress (σ_1) distribution

The σ_1 values reach magnitudes between 1.80 and 2.34 MPa in correspondence with specific geometric elements, including shared wall segments between adjacent chambers or pillars (cross-sections 1 to 3 in Figure 3.42, and cross-sections 1 to 5 in Figure 3.43), and sectors where chamber height decreases (cross-sections 1 and 2 in Figure 3.43). Comparable σ_1 values are also observed in proximity to discontinuity planes that lie near the section surface without fully intersecting it (as in Cross-section 5 in Figure 3.43), as

well as where discontinuities approach the external cliff façade surface or the bedding interface within the upper stratigraphic layers without cutting through them.

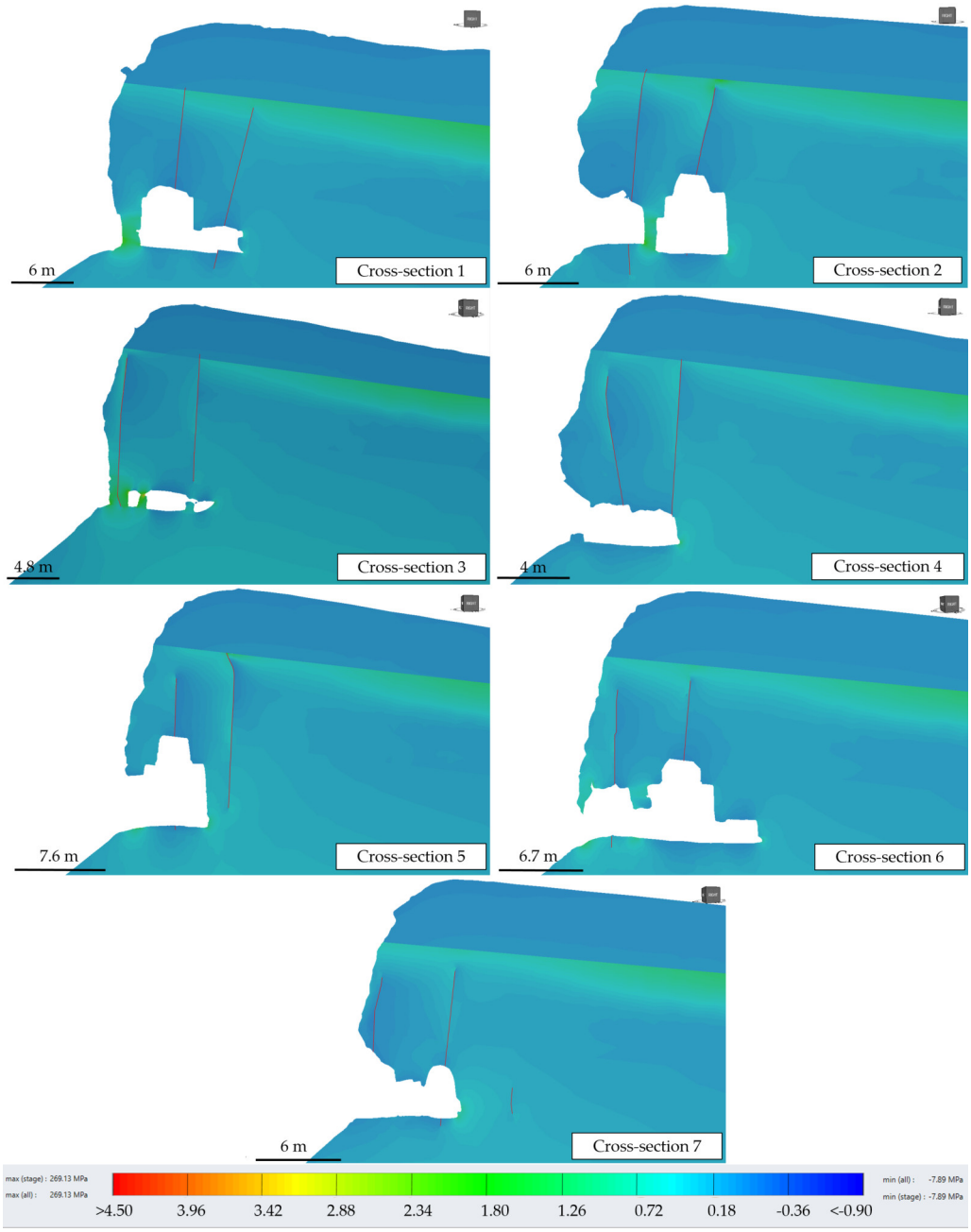

Figure 3.42: Set of seven cross-sections orthogonal to the cliff showing the major principal stress (σ_1) distribution.

Even if with low values, Figure 3.42 and Figure 3.43 highlight the influence on

discontinuities, both lithological boundaries and joins, on stress distribution as well as the shape and size of rock pillars and buttresses.

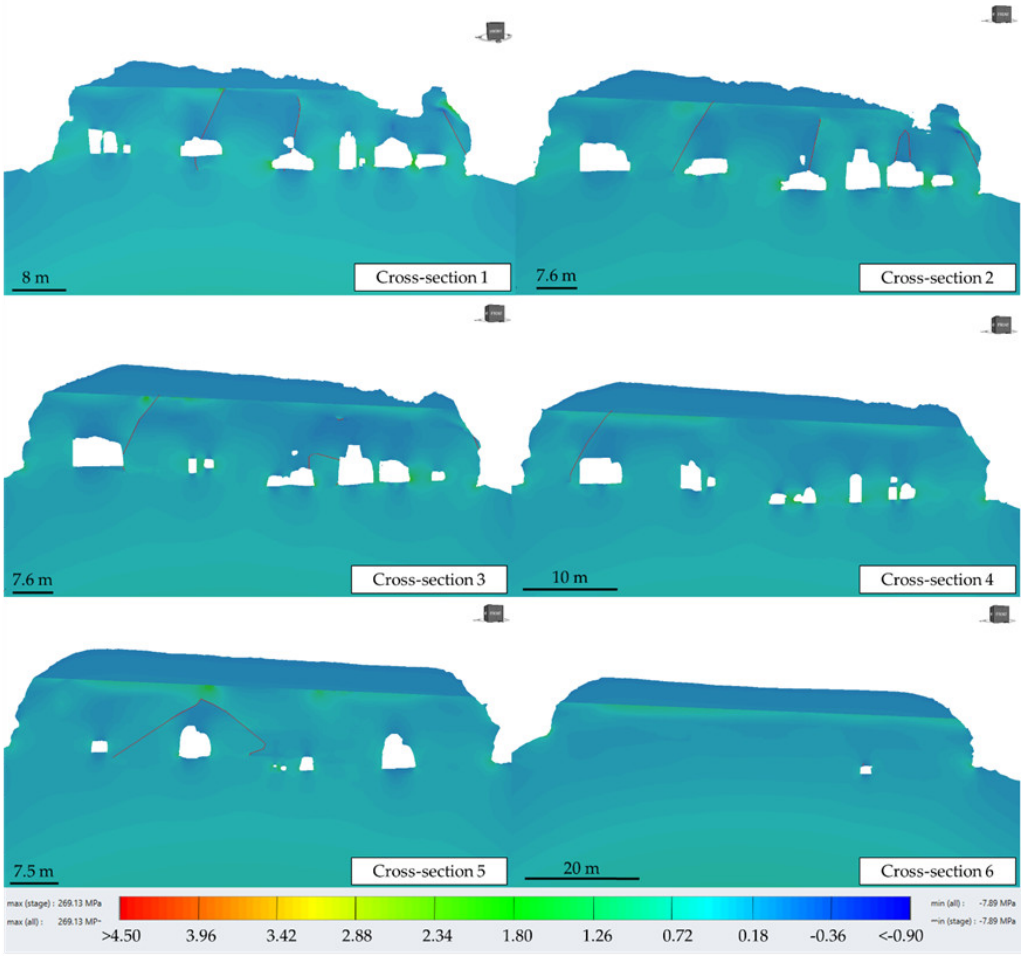

Figure 3.43: Set of six cross-sections parallel to the cliff showing the major principal stress (σ_1) distribution.

Shear stress (τ) distribution

An analogous spatial distribution is observed in the maximum shear stress (τ), where values reach up to 1.25 MPa adjacent to shared chamber walls or pillars (cross-sections 1 to 3 in Figure 3.44, and cross-sections 1 to 5 in Figure 3.45), sectors of reduced chamber height, and in correspondence with discontinuities that approach the external façade or bedding interfaces within the upper stratigraphic layers without fully intersecting them.

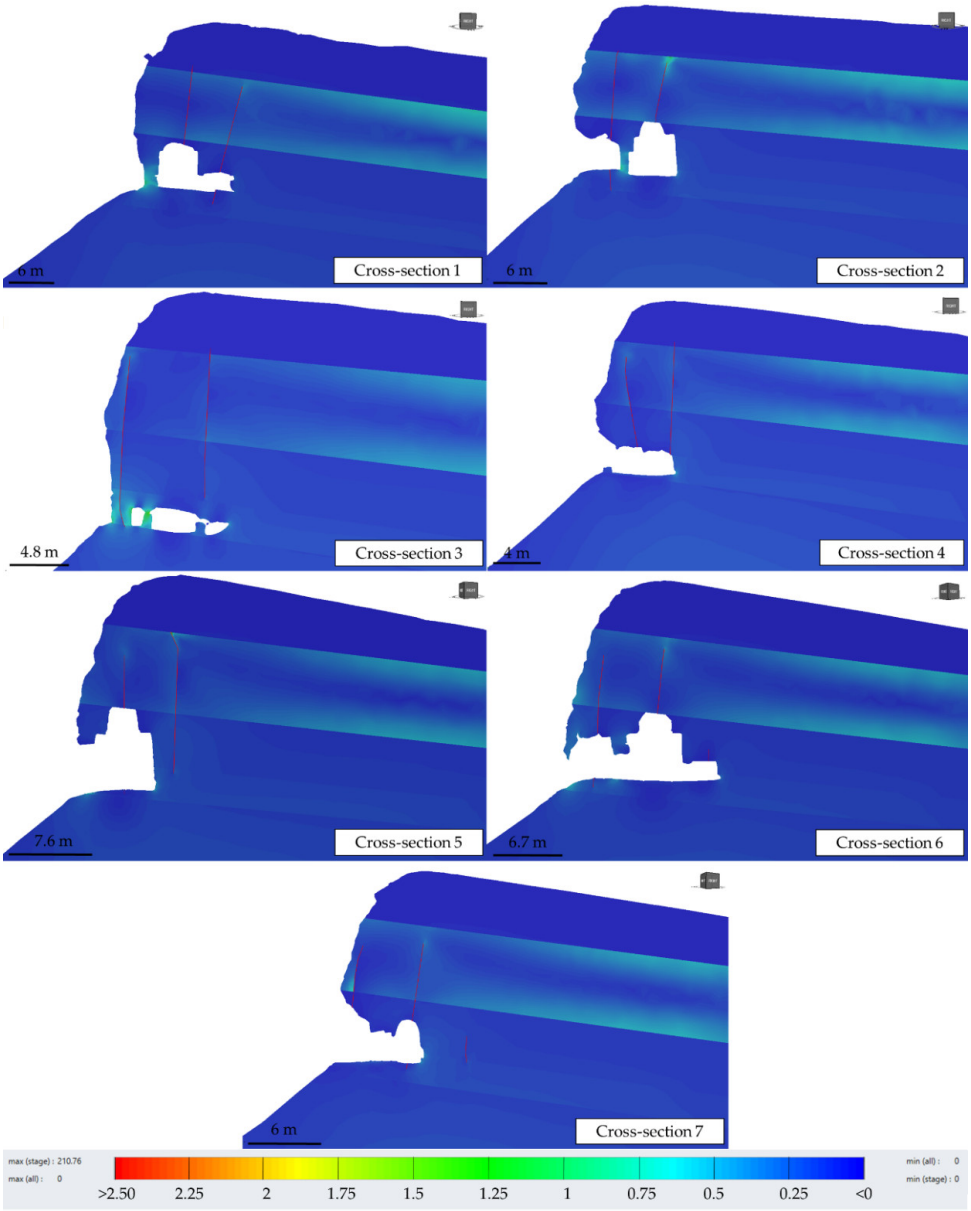

Figure 3.44: Set of seven cross-sections orthogonal to the cliff showing the shear stress (τ) distribution.

An analogous spatial distribution is observed in the maximum shear stress (τ), where values reach up to 1.25 MPa adjacent to shared chamber walls or pillars (cross-sections 1 to 3 in Figure 3.44, and cross-sections 1 to 5 in Figure 3.45), sectors of reduced chamber height, and in correspondence with discontinuities that approach the external façade or

bedding interfaces within the upper stratigraphic layers without fully intersecting them.

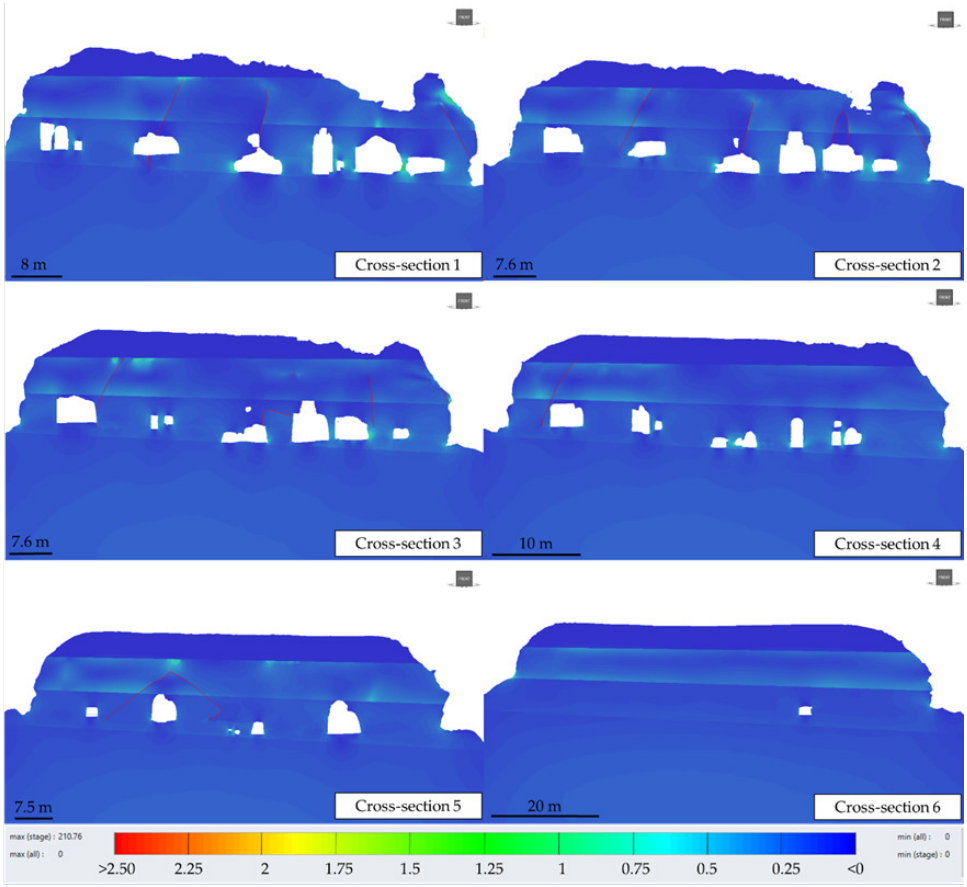

Figure 3.45: Set of six cross-sections parallel to the cliff showing the shear stress (τ) distribution.

Vertical displacement (u_z) distribution

The vertical displacement (u_z) pattern observed on the 3D model and across all cross-sections (Figures 3.46 and 3.47) is consistent between the external façade and the excavated cavities, with values degrading progressively toward $u_z \approx 0$ m at the basal clay horizon. The color maps show a smooth transition from negative displacements in rock volumes to neutral values in clay, with no visible internal disturbance or abrupt spatial displacement segmentation. The presence of discontinuities and bedding does not seem to influence the distribution of vertical displacements.

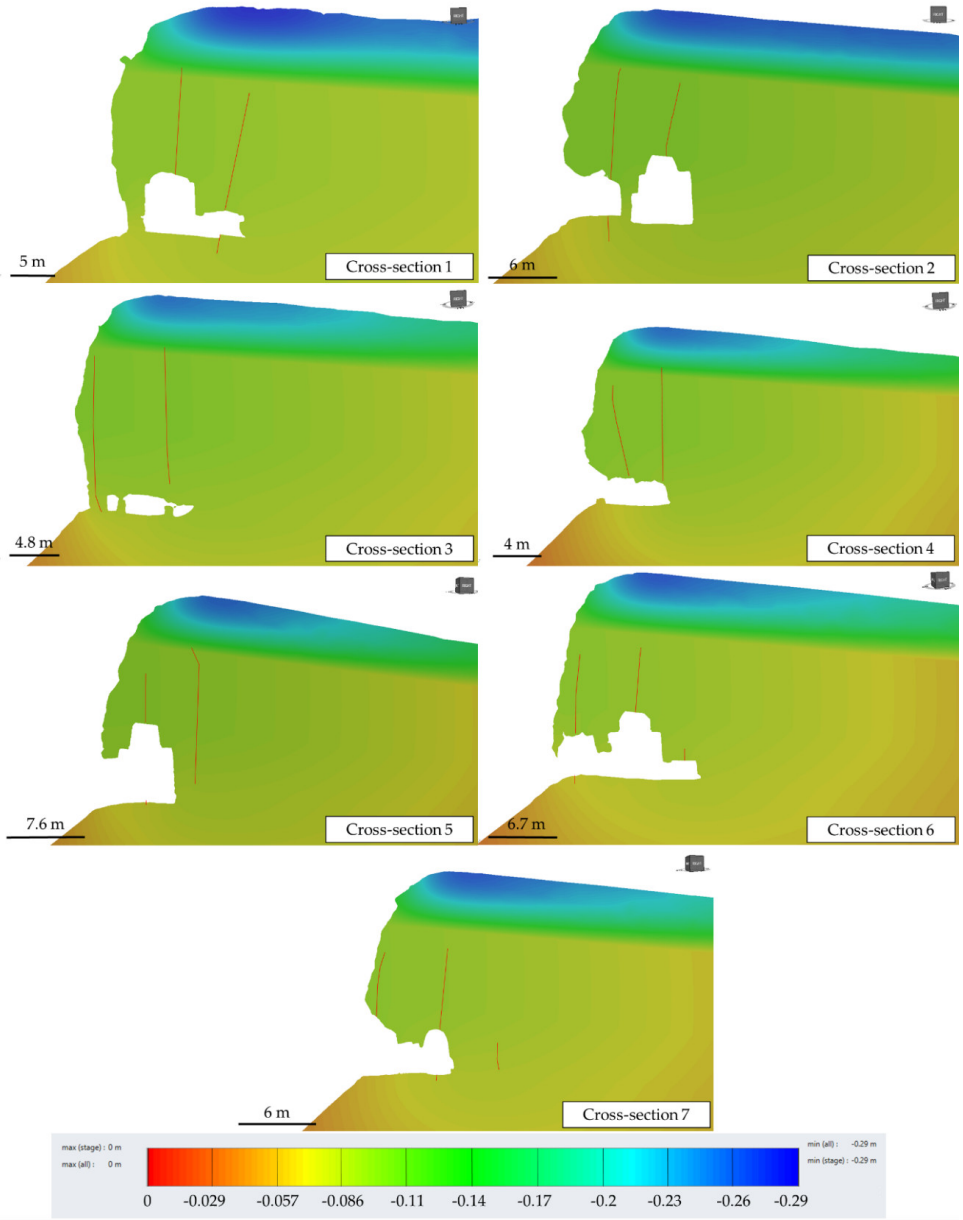

Figure 3.46: Set of seven cross-sections orthogonal to the cliff showing the shear stress (u_z) distribution.

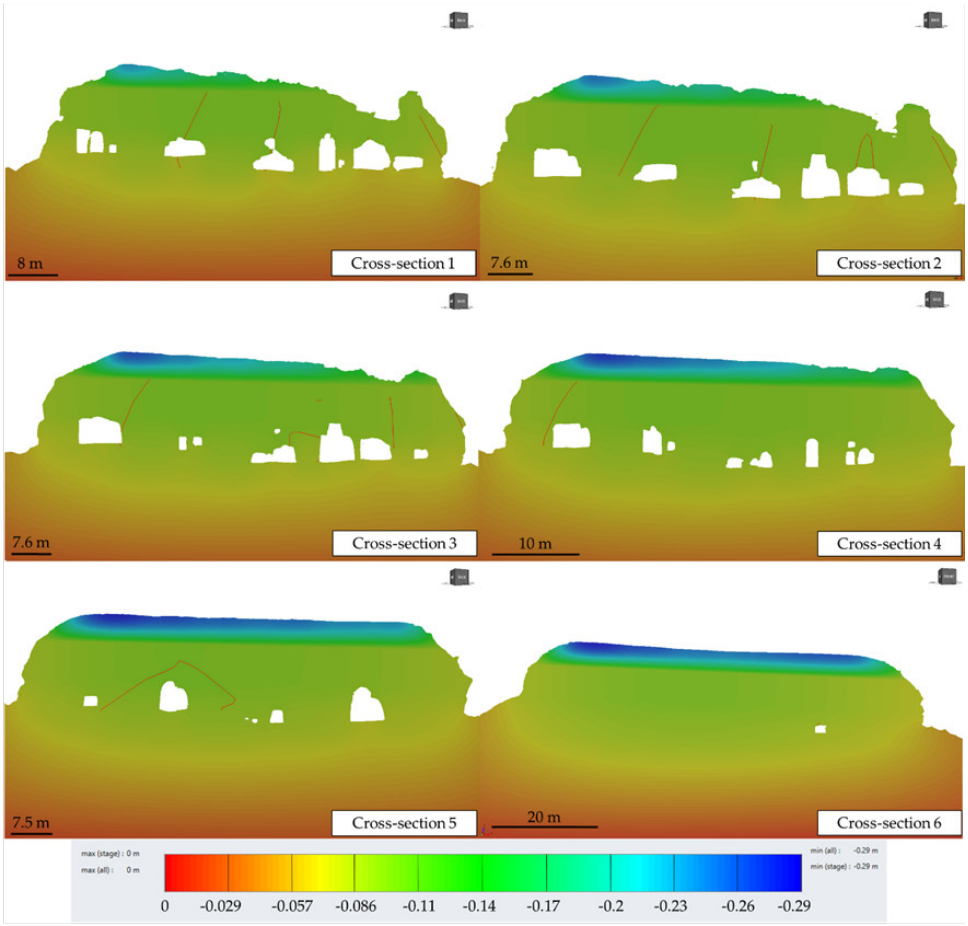

Figure 3.47: Set of six cross-sections parallel to the cliff showing the shear stress (u_z) distribution.

3.2.6 Discussion

Results of the multitemporal point cloud comparison (year 2018 – year 2025) highlight a clear pattern of surface degradation affecting the Sabereebi cliff. The volumetric analysis indicates that the façade is undergoing a dual-mode retreat process: (i) rare but structurally significant collapses, exemplified by block V1 (31.44 m^3), and (ii) widespread, low-magnitude detachments (V2–V11: 0.05–0.99 m^3) associated with granular disaggregation and progressive surface weakening. This degradation pattern reflects the intrinsic fragility of the lithological units that form the cliff, particularly the porous, weakly cemented sandstone and siltstone horizons.

In the composite σ_1 maps, stress magnitudes remain visually concentrated only in small geometry-constrained areas, primarily adjacent to reduced chamber heights and shared cavity-wall or pillar boundaries, while the surrounding façade intervals appear dominated by a continuous gradient without internal compressive stress clustering. A spatially analogous geometry-bounded pattern is observed in the τ field, where shear stresses also degrade continuously toward $\tau = 0$ MPa along the basal clay slope reference horizon, though the parameters express different mechanical components. As a benchmark for the scale of normal and shear stress magnitudes in similar lithologies, both σ_1 and τ values are framed using published intact-material strength ranges reported by **Marinos & Tsiambaos (2010)**. The model's highest normal stress and shear stress values influencing stability lie below typical intact failure thresholds for weak molasses sandstones and siltstones, respectively equal to 35.06 and 16.91 MPa. Notably, σ_1 values also remain below the more conservative strength value (14 MPa) adopted for sandstone in this study, further supporting the interpretation that the observed stress concentrations are not indicative of compressive failure but rather of geometry-controlled stress redistribution.

The structural discontinuities mapped across the façade act as preferential pathways for moisture infiltration and stress concentration, locally reducing the effective rock-bridges length and facilitating detachment. These observations are consistent with prior studies on the mechanical behavior and failure mechanisms of rock-cut complexes in southern Georgia and comparable rupestrian contexts (**Domej et al., 2022**; **Margottini et al., 2020**).

Climatic conditions in the Gareja semi-desert play a significant role in controlling the distribution of surface retreats. The alternation between intense daily thermal excursions, low atmospheric humidity, and episodic high-intensity rainfall promotes thermoelastic micro-fracturing and cyclic swelling–contraction of the rock matrix. In addition, salt crystallization within pore networks during wetting–drying cycles may contribute to the progressive breakdown of cementation, particularly in the siltstone and sandstone layers.

These processes align closely with the spatial clustering of small detachments around

carved chambers and architectural surfaces as documented in **Frullini (2022)** and **Frodella et al. (2021)**.

The concentration of detachments around cave entrances further indicates that anthropogenic excavation has introduced localized stress redistribution and exposed fresh rock surfaces to accelerated weathering. Overhang development, controlled by lithological contrasts between sandstone and underlying clay-rich levels, has contributed to the loss of natural structural support and the onset of slab detachment events such as V1 of Figure 3.31.

In recent years, temporary scaffolding structures have been installed in sectors where interior chambers open directly onto the external cliff face. These supports currently provide localized stabilization by reducing the risk of collapse at the junction between carved volumes and the retreating façade. However, the multitemporal comparison clearly shows that façade recession continues around and behind these interventions. Scaffolding, therefore, functions as a short-term protective measure, but it does not address the underlying drivers of instability—namely, infiltration along discontinuities, thermo-hygrometric stress, and clay-rich layer softening.

For this reason, stabilization strategies must extend beyond passive structural support and prioritize the management of surface water pathways at the top of the cliff. Non-intrusive micro-drainage solutions (e.g., shallow runoff deflection channels, reduced point infiltration, controlled water dispersion) have the potential to limit wetting–drying cycles and mitigate progressive weakening without altering the site's visual and architectural integrity. Continued multitemporal 3D monitoring remains essential for tracking the evolution of detachment volumes and identifying early warning indicators of instability.

In addition, future surveys at the site will require thoroughly engineering-geological data collection and rock sampling for new laboratory analysis that will allow a more reliable stress modelling. The future activities will include a dynamic simulation in such a way also to consider the seismic activity. Furthermore, new UAV and TLS acquisitions

will be functional for M3C2 new processing to investigate the progressive detachments and, if present, the impact of superficial water management.

To what concerns the FEM modeling, given the considerable number of estimated engineering-geological parameters, both of intact rock and discontinuities, a full sensitivity analysis will be essential to quantify the influence of parameter uncertainty on the model response. This analysis was not included at the moment as it exceeds the scope of the present study and will be addressed in a dedicated publication currently in preparation.

3.2.7 Conclusions

The present study illustrates a broad potential of integrating multitemporal 3D geomatic datasets with engineering-geological analysis to evaluate instability processes affecting rock-cut cultural heritage sites. The combined use of TLS, UAV-based photogrammetry, and M3C2 surface change detection proved effective in distinguishing between episodic block detachments and diffuse background weathering, while enabling a quantitative assessment of volumetric losses and spatial trends in cliff-face retreat.

The results suggest that more than stresses, degradation in soft-rock rupestrian environments arises from the interaction of multiple factors, including lithological heterogeneity, discontinuity patterns, and climate-driven thermo-hygrometric stresses. In such settings, cyclic wetting–drying, salt crystallization, and granular disaggregation tend to accelerate surface recession, particularly along carved architectural features and mechanically weak horizons. The multitemporal evidence demonstrates how gradual weakening can culminate in locally significant detachment events, underscoring the need for both diagnostic and predictive approaches.

While temporary stabilization measures can mitigate immediate hazards, they generally address the symptoms rather than the mechanisms of ongoing façade degradation. Effective long-term conservation therefore requires non-intrusive interventions aimed at

improving surface water management, limiting moisture fluctuations, and reducing thermally induced stresses, complemented by continued multitemporal 3D monitoring to support early-warning capabilities and informed maintenance planning.

More broadly, the methodological framework adopted here is transferable to other rock-cut or cliff-carved heritage contexts where geological fragility and cultural value coexist. By combining high-resolution surveying, quantitative change detection, and structural interpretation, it is possible to design conservation strategies that are scientifically robust, minimally invasive, and aligned with the sustainable preservation of vulnerable rupestrian heritage.

3.3 Analysis and monitoring of a vulnerable Vecchiano rock slope (Italy)

The present case study research and results were published in the following scientific manuscript: Beltramone, L., Rindinella, A., Vanneschi, C., & Salvini, R. (2024). Multitemporal Monitoring of Rocky Walls Using Robotic Total Station Surveying and Persistent Scatterer Interferometry. Remote Sensing, 16(20), 3848–3848. `https://doi.org/10.3390/rs16203848`

3.3.1 Introduction

Within the broader framework of this thesis, which investigates slope stability through advanced monitoring methodologies, this case study focuses on rockfall hazards and their mitigation in a high-risk setting.

Rockfalls represent one of the most hazardous slope processes, involving the sudden detachment and downslope movement of individual rock masses. Depending on morphology and triggering factors, these blocks may fall freely, bounce, roll, or slide along steep rock faces or cliffs. Their occurrence is controlled by a combination of geological structures and external drivers, including gravitational forces, mechanical and chemical weathering, freeze–thaw action, seismic activity, and anthropogenic disturbances (**Cruden & Varnes, 1996**; **Hungr, 2014**; **Varnes, 1978**). Such instabilities can cause damage at both local and regional scales, threatening infrastructure, transport corridors, and residential areas, as well as posing direct risks to human safety.

The danger of rockfalls stems from their rapid onset and unpredictable evolution, often occurring without detectable precursors. For this reason, understanding their mechanics and monitoring their dynamics are crucial steps toward effective risk reduction and the protection of exposed communities and assets. The development of monitoring systems

capable of providing early warnings and reliable risk assessments is therefore of primary importance.

Although rockfalls received comparatively limited scientific attention until the late 20^{th} century, research activity has significantly expanded since the early 2000s, driven by the increasing availability of innovative monitoring technologies and the recognition of their widespread hazard potential (**Briones-Bitar et al., 2020**).

Conventional approaches alone are often insufficient, as they may lack the spatial and temporal resolution required to capture the complexity of rockfall processes. Consequently, there is a growing interest in integrating advanced remote sensing methods with traditional field investigations to enhance the capacity for continuous and multitemporal monitoring (**Briones-Bitar et al., 2020**).

Current monitoring strategies can be broadly grouped into two categories: (i) remote sensing techniques, such as satellite photogrammetry, aerial and UAS—Unmanned Aerial System, aerial LiDAR—Light Detection and Ranging, and satellite interferometry (**Caliò et al., 2023**; **Konsolaki et al., 2024**; **Notti et al., 2022**; **Robiati et al., 2019**; **Schilirò et al., 2022**; **Vanneschi et al., 2022**; **Wang et al., 2023**; **Zhan et al., 2022**); (ii) ground-based monitoring systems, including ground-based LiDAR, ground-based interferometry, Doppler radar, RTS—Robotic Total Station surveying, distributed optical fiber sensors, geotechnical sensors (**Auflić et al., 2023**; **Barrias et al., 2016**; **Blahůt & Racek, 2023**; **Carlà et al., 2024**; **Carlino et al., 2016**; **Chen et al., 2024**; **Giacomini et al., 2020**; **Janeras et al., 2023**; **Lalam et al., 2016**; **Lanciano & Salvini, 2020**; **Lanciano et al., 2021**; **Lalam et al., 2016**; **Miles et al., 2020**; **Minardo et al., 2014**; **Minardo et al., 2018**; **Pasternak et al., 2023**; **Racek et al., 2021**; **Romeo et al., 2021**; **Salvini et al., 2015**; **Souza & Benoît, 2024**; **Wang et al., 2023**; **Zhan et al., 2022**; **Zhenglin et al., 2019**; **Zhenglin et al., 2022**).

The analysis of data can be done within GIS—Geographic Information Systems environment (**Castelli et al., 2021**; **Çelik & Gülersoy, 2017**; **Dematteis et al., 2022**;

Depountis et al., 2019; **El Miloudi et al., 2024**; **Pinto Santos et al., 2024**; **Wang et al., 2021**; **Wohlers & Damm, 2022**), and in models following numerical approaches (**Agliardi et al., 2024**; **Angın & Karahasan, 2024**; **Liu et al., 2024**; **Mahmood et al., 2024**; **Massaro et al., 2024**; **Noël et al., 2023**; **Peng et al., 2024**; **Yuen et al., 2023**).

These techniques allow for conducting both multitemporal and continuous monitoring, as well as data analysis, depending on site characteristics and monitoring budget. Methods offer distinct advantages, from large-scale coverage to high-precision point measurements, and their combined application allows for robust assessment of unstable slopes. In critical settings, these systems can also be coupled with early-warning and alert networks.

The present case study focuses on a sector characterized by vertical carbonate cliffs, with walls reaching heights of up to 80 m and extending for about 200 m. The outcrops are heavily fractured and weathered, largely due to pervasive karst processes. Previous rockfall events have led the Local Authority to classify the site as an area of high to very high geomorphological hazard. The presence of a public road and buildings in the proximity of the slope toe further emphasizes the need for continuous and reliable monitoring to mitigate future risks.

To achieve this, a multitemporal monitoring program was designed combining RTS surveys with satellite-based Persistent Scatterer Interferometry (PSI). The choice of methods was guided by (i) their high measurement accuracy relative to other optical or LiDAR-based techniques, (ii) the morphological characteristics of the cliffs, which hinder the use of distributed fiber optic sensors, and (iii) their relatively favorable cost compared to ground-based radar or extensive geotechnical instrumentation.

As a preparatory step, UAV surveys were conducted using nadiral and oblique acquisitions to generate a 3D point cloud and a detailed Digital Dense Elevation Model (DDEM). The latter supported geological photointerpretation of joints, blocks, and portions of walls that were considered unstable and were to be either monitored, removed, or secured with metal bolts and protection nets. In areas considered safe and accessible for personnel,

traditional engineering–geological surveys were also performed to characterize the rock mass and to conduct a slope kinematic stability analysis.

These studies were preparatory for setting the multitemporal monitoring system.

The prisms network for RTS monitoring was designed on the basis of these preliminary investigations, ensuring optimal line-of-sight, minimal human interference, and maximum safety for operators. The RTS was installed in a public space owned by the local administration, under controlled access, allowing continuous, high-precision monitoring of selected targets. However, given the intrinsic spatial limitations of RTS, complementary data from PSI analysis were employed. Using open-source processing chains and SAR imagery, PSI was employed to evaluate possible ground displacements in areas not visible from the RTS, particularly at the cliff tops, and provided information on the stability of the RTS installation area itself.

The integration of RTS and PSI thus combines the point-scale precision of terrestrial surveying with the large-scale coverage of satellite interferometry, yielding a comprehensive perspective on rockfall dynamics. By merging detailed displacement records with broader deformation patterns, this study contributes to an improved understanding of local instability processes and supports the design of proactive and effective hazard mitigation strategies.

In the context of this thesis, the case study exemplifies how the coupling of complementary monitoring systems can provide reliable and multi-scalar information for the assessment of slope stability. Alongside the other sites presented, it demonstrates the potential of integrated approaches to strengthen hazard evaluation and contribute to the development of more effective strategies for risk management in geomorphologically complex environments.

3.3.2 Geological setting

The study area is located in the eastern sector of the Vecchiano Municipality, in the Province of Pisa, Italy (Figure 3.48A). The rocky cliffs rise along the southwestern slopes of Monti d'Oltre Serchio and are mainly composed of limestones belonging to the "Calcare Massiccio" Formation, which is dated to the Hettangian–Lower Sinemurian period (**Boccaletti et al., 1969**; **Giannini & Nardi, 1965**; **Merla, 1952**; **Rau & Tongiorgi, 1969**; **Rau & Tongiorgi, 1974**). This stratigraphic unit can reach a thickness of up to 200 m and is characterized by light grey to pink limestones, commonly subdivided into two distinct microfacies that reflect deposition in a shallow-water carbonate platform environment (**Boccaletti et al., 1969**).

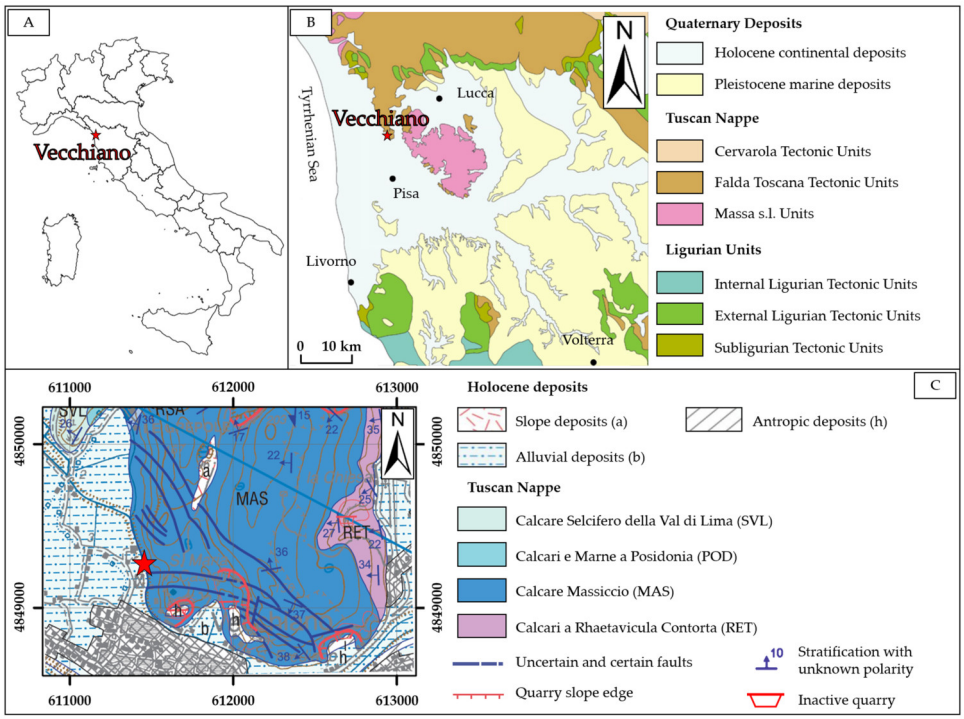

Figure 3.48: Geology of the investigated area. (A) General location of the site in Italy; (B) regional setting based on Sheet no. 273 "Pisa," adapted from **Carosi et al., 2021**; (C) extract of the same geological sheet (**Carosi et al., 2021**). The study site is highlighted with a red star.

From a structural standpoint, the Monti d'Oltre Serchio sector represents the out-

come of a prolonged geodynamic interaction between the Adria microplate and the Corso–Sardinian block (**Carosi et al., 2021**). In this context, the area exposes lithostratigraphic units of the non-metamorphic Tuscan Nappe, which range in age from the Upper Triassic to the Upper Oligocene and are tectonically detached from the underlying metamorphic basement (Figure 3.48B).

The tectonic framework of Vecchiano is largely influenced by synthetic NW–SE trending extensional faults that developed between the Middle Pliocene and the Upper Pleistocene (Figure 3.48C; **D'Amato & Nardi, 1993**). These structures strongly conditioned the morphology of the area, producing a steep escarpment approximately 200 m in height and oriented NNW–SSE, which separates the summit of the slope from the adjacent alluvial plain (**D'Amato & Nardi, 1993**).

In addition to tectonic processes, karst phenomena such as dolines and sinkholes are widespread. These features significantly affect both surface morphology and subsurface hydrology, further enhancing the geomorphological complexity of the area and influencing groundwater circulation patterns (**Carosi et al., 2021**).

3.3.3 Material and Methods

The comprehensive analysis of the present case study integrates both geological surveys and multitemporal monitoring methods. The geological component included topographic, photogrammetric, and in situ engineering–geological surveys, combined with slope photointerpretation, rock mass characterization, and statistical kinematic stability analysis (Sections 3.3.3.1 - 3.3.3.4).

The multitemporal monitoring was based on Robotic Total Station (RTS) surveys and Persistent Scatterer Interferometry (PSI) (Sections 3.3.3.5 - 3.3.3.6).

Figure 3.49 shows the overall methodology flowchart.

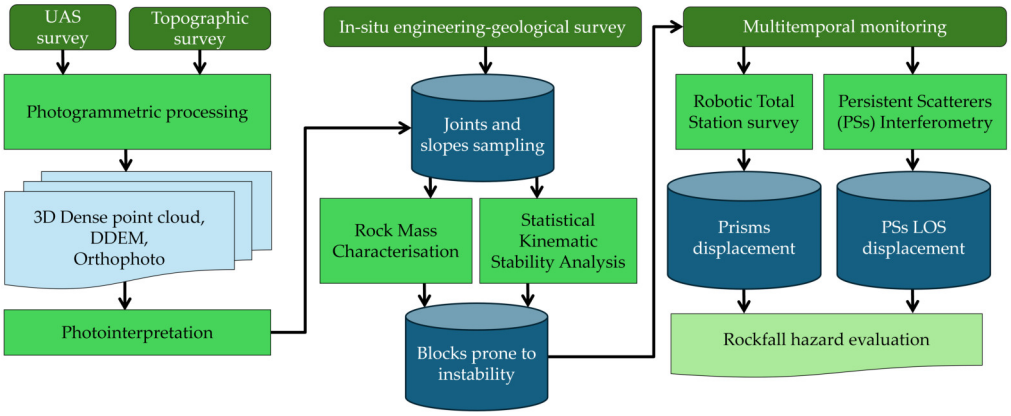

Figure 3.49: Overall methodology flowchart.

The topographic and photogrammetric surveys were designed to produce a 3D model that was useful not only for identifying elements prone to instability but also for characterizing the discontinuity systems at the slope scale. These data, together with the results of the engineering–geological surveys, were used to conduct the kinematic slope stability analysis. Geological survey data also allowed for the definition of potentially unstable rock blocks, wall portions, and pinnacles, which were selected for the installation of monitoring prisms (Section 3.3.3.5). Multitemporal monitoring was conducted periodically over a 2-year span in collaboration with the Tuscany and Umbria Regional Directorate of the State Property Agency, which funded the research. The PSI analysis was employed to assess displacements at the top of the slopes in areas not visible from the RTS.

3.3.3.1 Topographic survey

The topographic survey was performed with a Leica™ Viva GS15 dual-frequency geodetic GNSS receiver and a Leica™ Nova MS50 RTS (angular accuracy of 1″ and distance accuracy of 1 mm + 1.5 ppm) (Figure 3.50).

The GNSS survey aimed at georeferencing artificial markers used for the exterior orientation of images acquired by the UAS photogrammetric survey. Real-Time Kinematic (RTK) positioning was applied with a minimum acquisition time of 30 seconds per marker

and a 1 second observation rate. Orthometric heights of markers were later calculated using ConverGo software (**CISIS, 2012**).

Figure 3.50: Stages of the GNSS (A) and RTS surveys (B).

Two temporary reference points were also measured, in terms of absolute coordinates, to georeference the RTS system. These points were surveyed in static mode for about 3 hours and processed with Leica Geosystems^{TM} Infinity software (Version 3.4.2; **Leica Geosystems^{TM} AG, 2021**) using differential methods and simultaneous records from the SmartNet ItalPos national GNSS network. This ensured sub-centimetric accuracy, allowing the RTS survey to be rotated and shifted into a georeferenced system, which was also used for cartographic purposes.

Prior to the execution of the topographic survey, a preliminary inspection was conducted in coordination with the Tuscany and Umbria Regional Directorate of the State Property Agency, with the objective of identifying the most suitable location for the installation of the RTS reference base. Consequently, a site at the base of the rock slope was strategically selected, providing an unobstructed line of sight towards the prisms to be installed on the slope (Figure 3.50B).

3.3.3.2 UAS photogrammetric survey

The photogrammetric survey covered ~ 18 ha using a DJI™ Mavic 2 Pro drone equipped with a Hasselblad® L1D-20C camera (20 MP, 1-inch sensor, 10.26 mm lens). Six manual flights and one nadiral automated flight, planned in UgCS software (Version 4.18; **SPH Engineering, 2023**), were conducted, resulting in 426 high-resolution images (GSD-Ground Sampling Distance = 2.8 cm).

Images were externally oriented and processed using Agisoft™ Metashape software (Version 2; **Agisoft LLC, 2023**) through Structure-from-Motion (SfM) and Multi-View Stereo (MVS) techniques. Alignment relied on 9 Ground Control Points (GCPs) and 4 Check Points (CPs), plus 5 GCPs measured by RTS on vertical rock walls.

3.3.3.3 Engineering–geological survey and rock mass characterization

In situ surveys were conducted in safe, accessible portions of the rock walls (Figure 3.51A and 3.51B).

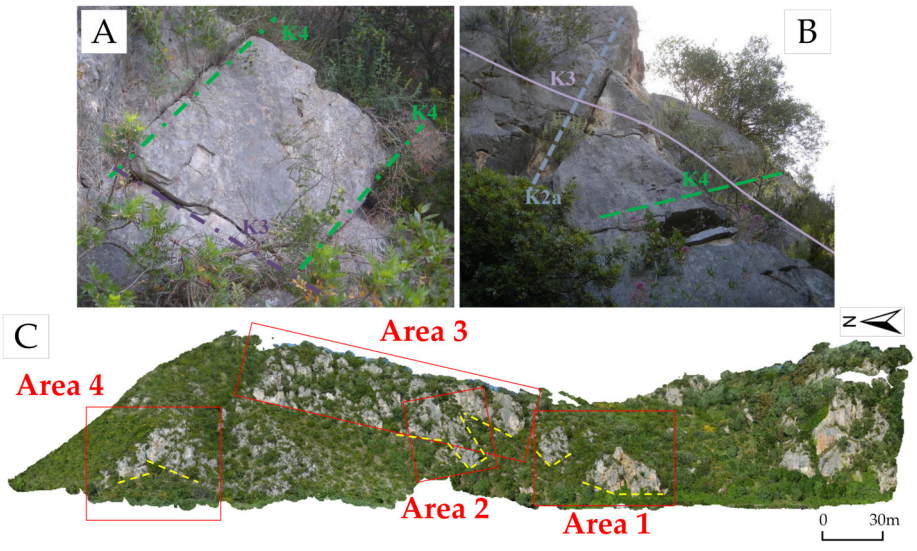

Figure 3.51: Images in panels (A) and (B) illustrate representative outcrops chosen for the in situ engineering–geological investigations. In panel (C), yellow dashed lines mark the position of the scanlines along the slope, while red rectangles highlight the portions of rock mass where discontinuity sampling was carried out using CloudCompare software.

Additional joint sampling, indicated in red in 3.51C, was conducted directly on the 3D point cloud using the Plane Tool plugin of CloudCompare software (Version 2; **CloudCompare, 2021**).

The final dataset, available for rock mass classification and slope stability kinematic statistical analysis, is represented by a total of 237 joints.

The data collected from the in situ engineering–geological survey includes information such as discontinuity orientation, spacing, persistence, aperture, type and thickness of infilling, roughness and JRC—Joint Roughness Coefficient (derived from profilometer tests), weathering, humidity, and indirect uniaxial compressive strength (derived from the Schmidt hammer rebound tests).

Rock mass classification was performed using the Rock Mass Rating (RMR) method (**Bieniawski, 1989**) and the Slope Mass Rating (SMR) method (Romana, 1985). Both methodologies are based on the calculation of a rating derived from the analysis of discontinuity system data; these ratings define a specific class of rock or slope mass quality and, in turn, indicate the potential need for support or reinforcement measures. The adoption of both approaches was deemed appropriate to achieve a more comprehensive characterization of the site, encompassing not only the rock mass quality but also the geometrical factors influencing slope stability.

In particular, the SMR method, which builds upon the basic RMR value (RMRb), is specifically designed for evaluating rock slope stability, as it integrates additional parameters such as slope orientation, joint attitudes, and their mutual relationships. For this purpose, the slopes analyzed within the SMR framework were delineated using the 3D point cloud generated through the aerophotogrammetric survey.

3.3.3.4 Statistical slope stability kinematic analysis

The kinematic stability analysis focuses on the geometric relationships and potential failure modes of individual rock blocks or masses within a slope. This type of assessment

is fundamental in geotechnical engineering for evaluating the stability of both natural and engineered slopes. Rock blocks are defined by discontinuities or planes of weakness, such as joints, faults, bedding planes, or other geological features.

Through this methodology, potential failure mechanisms can be identified by analyzing the kinematic behavior of the blocks. The approach considers possible failure surfaces along which sliding or rotation may develop, enabling the prediction of failure modes and the conditions under which instability is likely to occur.

In this study, the analysis was conducted using stereonet projections following the method proposed by **Markland, 1972** and subsequently revised by **Hoek & Bray, 1981**. This technique highlights the main kinematic mechanisms, including planar sliding, wedge sliding, and different forms of toppling (direct, oblique, and flexural). The likelihood of failure is controlled not only by the interaction between joint sets and slope orientation but also by the condition in which the shear strength of the rock mass is exceeded, particularly when the friction angle (ϕ) is surpassed.

For this case study, joint data derived from the engineering–geological field survey, complemented by photointerpretation of UAS-acquired imagery, were employed to identify and characterize the discontinuities. These data were subsequently used for a statistical slope kinematic stability assessment conducted thanks to Rocscience^{TM} Dips software (Version 8.022; **Rocscience, 2022**).

3.3.3.5 Multitemporal monitoring through RTS

The multitemporal monitoring campaign consisted of eight RTS surveys in addition to the initial baseline measurement, referred to as Survey n.0, and it spanned a period of approximately two years. The monitoring activities started in February 2020, prior to the COVID-19 pandemic, and subsequent surveys were scheduled in compliance with health and safety guidelines. The origin point of the monitoring network was established on an iron plate specifically designed to bear the instrument's weight, which was anchored to a